Journal of Materials Chemistry A

ROYAL SOCIETY OF CHEMISTRY

PAPER

Published on 26 August 2026
Licence and permissions

Cite this: DOI: 10.1039/d6ta05865e

Sulfonated anthraquinone (PPAAQS) as robust organic cathode for long-term zinc-ion battery

Shuyang Bian,†[a] Fei Ye,†[b] Zhehao Zhang,[a] Peilin Liang,[a] Yu Chen,[a] Runmo Wang,[a] Yuping Wu[cd] and Linfeng Hu *[ad]

Received 13th July 2026
Accepted 24th August 2026

DOI: 10.1039/d6ta05865e

rsc.li/materials-a

Organic cathode materials for aqueous zinc-ion batteries (AZIBs) offer inherent advantages in structural tunability and sustainability, yet their practical deployment is largely hindered by sluggish reaction kinetics and inadequate cycling durability. Here, we report a sulfonated anthraquinone-based polymer (PPAAQS) as a high-performance AZIB cathode *via* a molecular sulfonation strategy, wherein the incorporated sulfonic acid groups concurrently modulate the electronic structure and facilitate ion transport. Density functional theory calculations reveal that sulfonation lowers the lowest unoccupied molecular orbital (LUMO) energy level and strengthens Zn^{2+} binding with carbonyl active sites, thereby promoting charge transfer and redox kinetics. Meanwhile, the hydrophilic sulfonated framework enhances electrolyte wettability and accelerates both Zn^{2+} migration and proton-coupled electron transfer processes. Consequently, the PPAAQS cathode delivers superior rate capability and outstanding long-term cycling stability, retaining 80.4% of its initial capacity after 7100 cycles. This work establishes an effective electron/ion dual-regulation paradigm *via* molecular sulfonation engineering and offers fresh insights into the rational design of durable organic cathodes for aqueous zinc-ion batteries.

Introduction

Aqueous zinc-ion batteries (AZIBs) have emerged as promising candidates for large-scale energy-storage applications owing to their high safety, low cost, environmental benignity, and the high theoretical capacity of Zn metal anodes.[1–4] Despite these advantages, the development of high-performance cathode materials remains a major challenge that limits the practical implementation of AZIBs. To date, various inorganic cathodes, including Mn-based oxides, V-based compounds, and Prussian blue analogues, have been extensively investigated.[5–8] However, these materials generally suffer from structural instability, sluggish Zn^{2+} diffusion, and unsatisfactory cycling durability.[9–11] Therefore, exploring alternative cathode materials with tunable structures and favorable reaction kinetics is highly desirable.

Organic electrode materials have attracted increasing attention for their structural diversity, sustainability, and molecular designability.[12–15] Among them, carbonyl-based compounds, particularly anthraquinone derivatives with multiple redox-active sites and extended π-conjugation, show considerable promise as AZIB cathodes.[16,17] Polymerization strategies have been developed to mitigate the dissolution of small-molecule analogues, substantially improving cycling stability.[18,19] However, anthraquinone-based polymers still suffer from intrinsic limitations:[17,20,21] localized carbonyl electronic structures cause sluggish charge transfer and underutilized active sites; poor electrolyte affinity and ion transport impede Zn^{2+} migration; and strong Zn^{2+}-carbonyl electrostatic interactions induce high diffusion barriers and severe polarization at high rates. Therefore, simultaneously achieving fast charge-transfer kinetics, efficient ion transport, and long-term durability remains a critical challenge for anthraquinone polymer cathodes.

Molecular functionalization presents a potent strategy for concurrently regulating the electronic structure and ion-storage behavior of polymer cathodes.[22] Among diverse functional groups, sulfonic acid groups ($-SO_3H/-SO_3^-$) have recently been utilized in aqueous zinc-ion batteries. Nevertheless, their functions are still mostly fragmented. They act either as Zn^{2+}-conductive channels, proton buffers, or interfacial modifiers, without integrating their electron-withdrawing, ion-transport, and proton-reservoir capabilities into a unified design.[23–25] The electron – withdrawing effect of sulfonic acid groups can reduce the lowest unoccupied molecular orbital (LUMO) level of carbonyl compounds and expedite electron transfer. Meanwhile, the polar sulfonated moieties improve wettability, encourage Zn^{2+} adsorption, and establish ion-transport pathways. More significantly, the proton-rich characteristic of

[a]School of Materials Science and Engineering, Southeast University, Nanjing 211189, P. R. China. E-mail: linfenghu@seu.edu.cn
[b]Nanjing Polytechnic Institute, Nanjing 210044, P. R. China
[c]School of Energy and Environment, Southeast University, Nanjing 211189, P. R. China
[d]Z Energy Storage Center, Southeast University, Nanjing 211189, P. R. China
† These authors contributed equally: Shuyang Bian, Fei Ye.

sulfonic acid groups might facilitate proton-coupled electron transfer, a crucial kinetic process in aqueous zinc-organic batteries. To date, however, there is still a lack of a systematic demonstration of how sulfonation simultaneously realizes electron regulation, reversible proton participation, and synergistic dual-ion transport in polymer cathodes, despite the obvious potential of such an integrated approach.

Inspired by these considerations, a sulfonated anthraquinone polymer (PPAAQS) is developed as a cathode material for AZIBs, while the non-sulfonated polymer (PPAAQ) is employed as a control sample. Benefiting from the synergistic regulation of electronic structure and ion transport induced by sulfonic acid groups (Scheme 1b), PPAAQS exhibits significantly enhanced electrochemical activity, accelerated Zn^{2+} storage kinetics, and superior cycling stability. Combined experimental and theoretical investigations reveal that sulfonation effectively lowers the LUMO energy level, enhances Zn^{2+} affinity, improves electrolyte wettability, and facilitates ion diffusion. This work demonstrates an effective electron/ion dual-regulation strategy for carbonyl-based organic cathodes and provides new insights into the molecular design of high-performance organic electrode materials for durable aqueous zinc-ion batteries.

Results and discussion

The synthetic route of poly (pyromellitic anhydride-*alt*-anthraquinone) (PPAAQ) and poly (pyromellitic anhydride-*alt*-anthraquinone sulfonate) (PPAAQS) material is schematically illustrated in Scheme 1a. Pyromellitic dianhydride (PMDA) was reacted with anthraquinone (AQ) and sodium anthraquinone-1-sulfonate (AQS), respectively, in an $AlCl_3$/NaCl molten salt medium.[26] The reaction mixture was heated at 250 °C under continuous stirring for 2 h, yielding black powdered PPAAQ and PPAAQS products. Notably, the PPAAQS sample (inset in Fig. 2a) was further purified *via* acidification, with the detailed procedure provided in the Experimental Section. Fourier transform infrared spectroscopy (FT-IR) was employed to verify the successful fabrication of PPAAQ and sulfonic acid-functionalized PPAAQS (Fig. 1a and S1). For PPAAQS, two characteristic stretching vibration peaks assigned to the quinone carbonyl group (C=O) were observed at 1610 and 1670 cm^{-1}.[27] The characteristic absorption peak at ~1570 cm^{-1} corresponded to the skeletal stretching vibration of aromatic C=C bonds.[28] Furthermore, the absorption peaks at ~1250 cm^{-1} was attributed to the stretching vibrations of S=O bonds in sulfonic acid groups, respectively.[29] In contrast, no S=O bond characteristic signals were detected in the PPAAQ spectrum, whereas the characteristic vibration peaks of quinone carbonyl groups and aromatic ring skeletons were well preserved (Fig. S1). Combined with elemental analysis results (Table S1), the introduction of sulfonic acid groups into the polymer framework is confirmed by multiple independent techniques. The X-ray diffraction (XRD) pattern (Fig. 1b and S2) reveals two major broad diffraction peaks around 25° and 43°, indicative of the amorphous structure of the π-conjugated polymers PPAAQ and PPAAQS. No obvious sharp diffraction peaks are observed, which reflects the absence of long-range crystalline ordering.[30] The results of thermogravimetric analysis (TGA) (Fig. S3) demonstrate that the incorporation of sulfonic acid groups into the main polymer chain does not impair the intrinsic thermal stability of PPAAQS, and moreover can further improve it.

X-ray photoelectron spectrometer (XPS) analysis was performed to further characterize the surface chemical composition of PPAAQS. The high-resolution C 1s spectrum was (Fig. 1c) deconvoluted into three distinct components. The dominant peak at ~284.2 eV corresponds to the C–C/C–H bonds of the aromatic polymer framework. The component at ~285.7 eV is assigned to the carbonyl (C=O) moieties derived from the anthraquinone and pyromellitic anhydride units.[12] Notably, a small additional peak at ~288.2 eV, attributed to the C–S bonds, confirms the successful incorporation of sulfonate groups into the polymer backbone. The O 1s spectrum (Fig. S4) further supports the structural composition, showing three characteristic peaks. The peak at ~532.2 eV corresponds to the quinone carbonyl (C=O) groups, while the signal at ~533.5 eV is attributed to C–O species in the polymer. Importantly, a high-binding-energy component at ~535.8 eV is observed, which is characteristic of the S=O bonds in sulfonic acid ($-SO_3^-$) groups.[31] The characteristic doublet of sulfonate groups at ~163.1 eV (S $2p_{3/2}$) and ~164.2 eV (S $2p_{1/2}$). is unequivocally verified by the S 2p spectrum (Fig. 1d).

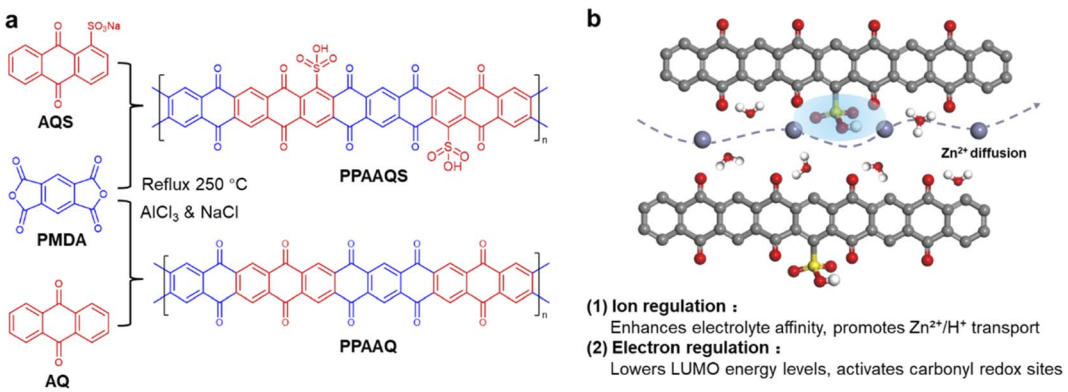

Scheme 1 (a) Synthesis route of PPAAQ and PPAAQS. (b) Electron-ion regulation mechanism of sulfonic acid groups of PPAAQS.

 This journal is © The Royal Society of Chemistry 2026

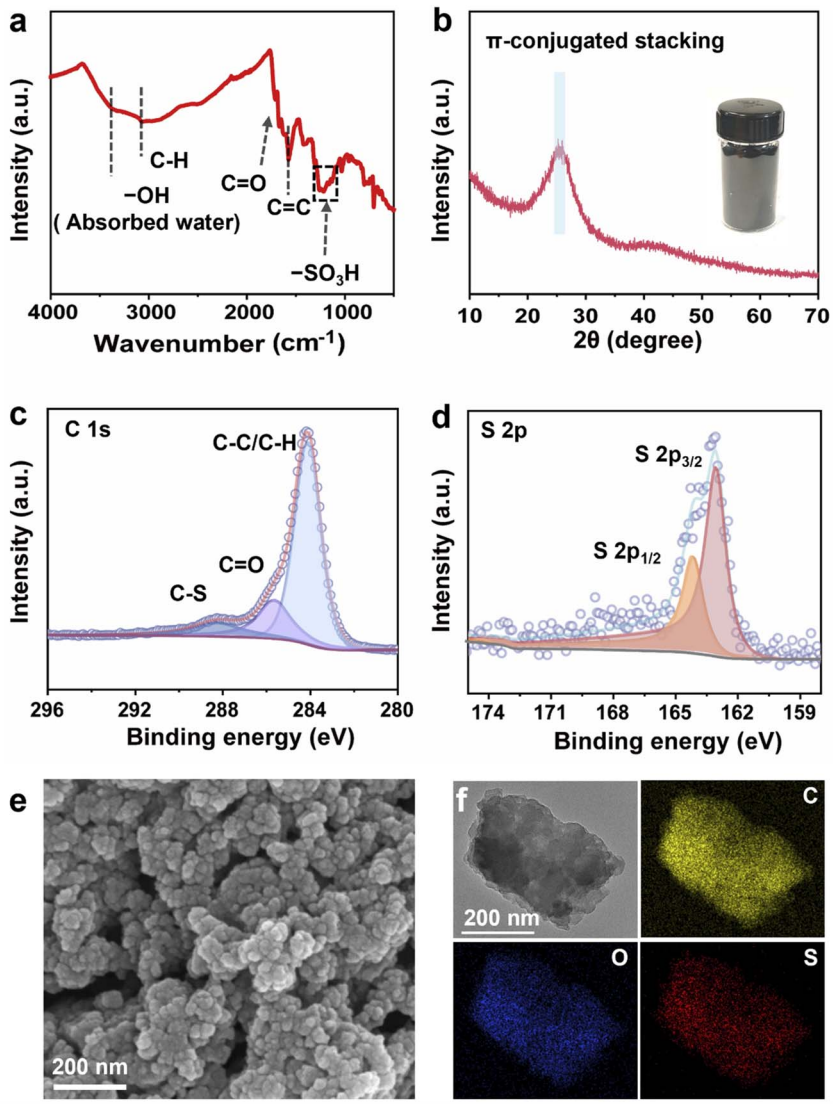

Fig. 1 Characterization of PPAAQS: (a) FTIR spectrum, (b) XRD pattern (inset: PPAAQS powder sample), and high-resolution XPS spectra of (c) C 1s and (d) S 2p. (e) SEM image, (f) TEM image, and corresponding EDS elemental mappings of C, O, and S.

Furthermore, the morphology and microstructure of the PPAAQS and PPAAQ were investigated by scanning electron microscopy (SEM) and transmission electron microscopy (TEM). As shown in Fig. 1e, S5 and S6, the SEM image reveals that PPAAQS and PPAAQ consists of aggregated nanoparticles. The TEM image (Fig. 1f) further confirms the aggregated morphology of the polymer. Elemental mapping by energy dispersive X-ray spectroscopy (EDS) reveals the uniform distribution of C, O, and S elements throughout the sample, demonstrating that sulfonic acid groups are homogeneously incorporated into the polymer framework.

The electrochemical performance was evaluated in coin-type cells using AQ/AQS monomers, PPAAQ, or PPAAQS as the cathode, Zn foil as the anode, and 2.0 M aqueous $ZnSO_4$ as the electrolyte (Fig. 2a). The cyclic voltammetry (CV) curves of the AQ and AQS monomers are presented in Fig. S7. The AQ monomer exhibits a single pair of redox peaks at 0.37 V and 0.69 V, corresponding to a one-step two-electron redox reaction during Zn^{2+} storage; however, a distinct oxygen evolution reaction (OER) is observed at high potentials. In comparison, the sulfonated AQS monomer exhibits a pair of redox peaks positively shifted to approximately 0.45 and 0.96 V, accompanied by significantly suppressed OER behavior. The positive shift of the redox potential indicates that the introduction of the electron-withdrawing sulfonic acid groups effectively regulates the electronic structure of the anthraquinone unit and alters the thermodynamics of the carbonyl redox reaction.[32] Meanwhile, the suppressed OER suggests improved electrode stability in aqueous electrolyte. Nevertheless, the practical application of AQ and AQS is still hindered by the intrinsic dissolution of small-molecule organic electrodes, which inevitably leads to rapid capacity fading and poor cycling stability (Fig. S8).[14]

Therefore, to overcome this limitation, we reacted AQ and AQS with PMDA monomer *via* condensation to obtain more

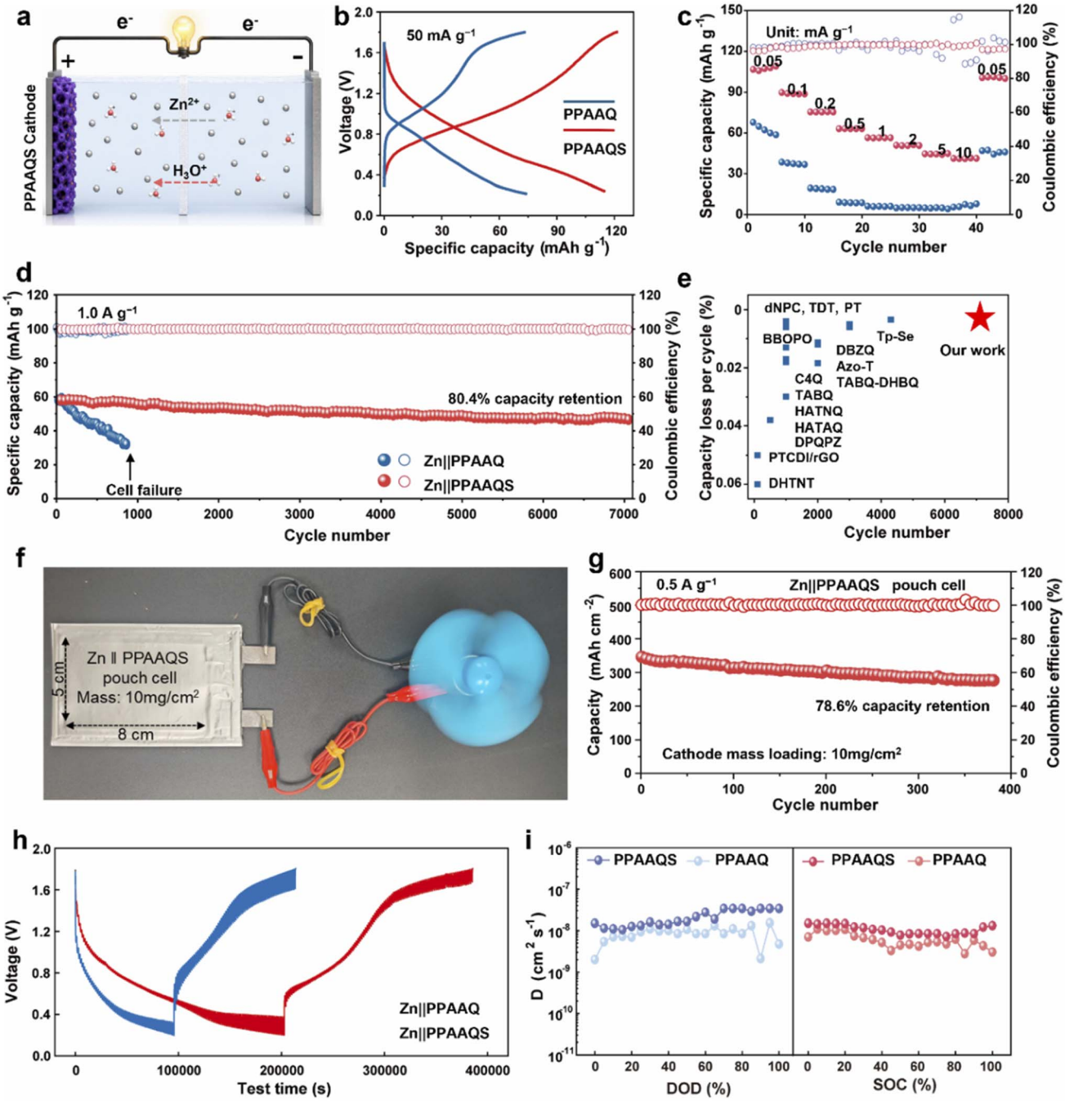

Fig. 2 (a) Schematic illustration of Zn||PPAAQS ZIBs configurations. (b) GCD curves, (c) rate-performance, and (d) long-term cycle performance of Zn||PPAAQ and Zn||PPAAQS cell. (e) Comparison of the capacity retention and cycle between the PPAAQS electrode and reported organic cathodes. (f) Optical image of 8 × 5 cm Zn||PPAAQS pouch cell (active mass loading: 10 mg cm^{-2}) lighting a small fan. (g) Long-term cycling of Zn||PPAAQS pouch cell at 0.5 A g^{-1}. (h) GITT curves of PPAAQS and PPAAQ during one discharge/charge cycle. (i) The corresponding Zn^{2+} ion diffusion coefficient ($D_{Zn^{2+}}$) at different depth of discharge (DOD) and state of charge (SOC).

stable polymers (PPAAQ and PPAAQS). As shown in Fig. S9, PPAAQS exhibits two pairs of redox peaks located at approximately 0.47/0.72 V and 0.85/1.05 V. The low-potential redox couple can be assigned to the reversible conversion between carbonyl and enolate species accompanied by Zn^{2+} coordination, while the origin of the high-potential redox couple was further investigated through electrolyte-dependent CV measurements (Fig. S10). When the $ZnSO_4$–H_2O electrolyte was replaced by a $ZnSO_4$–ACN (acetonitrile) electrolyte, the high-potential redox feature became significantly weakened whereas the low-potential redox peaks remained largely preserved (Fig. S10b). Moreover, the high-potential redox response was still retained in aqueous Zn^{2+}-free Na_2SO_4 electrolytes and became more pronounced under acidic conditions

This journal is © The Royal Society of Chemistry 2026

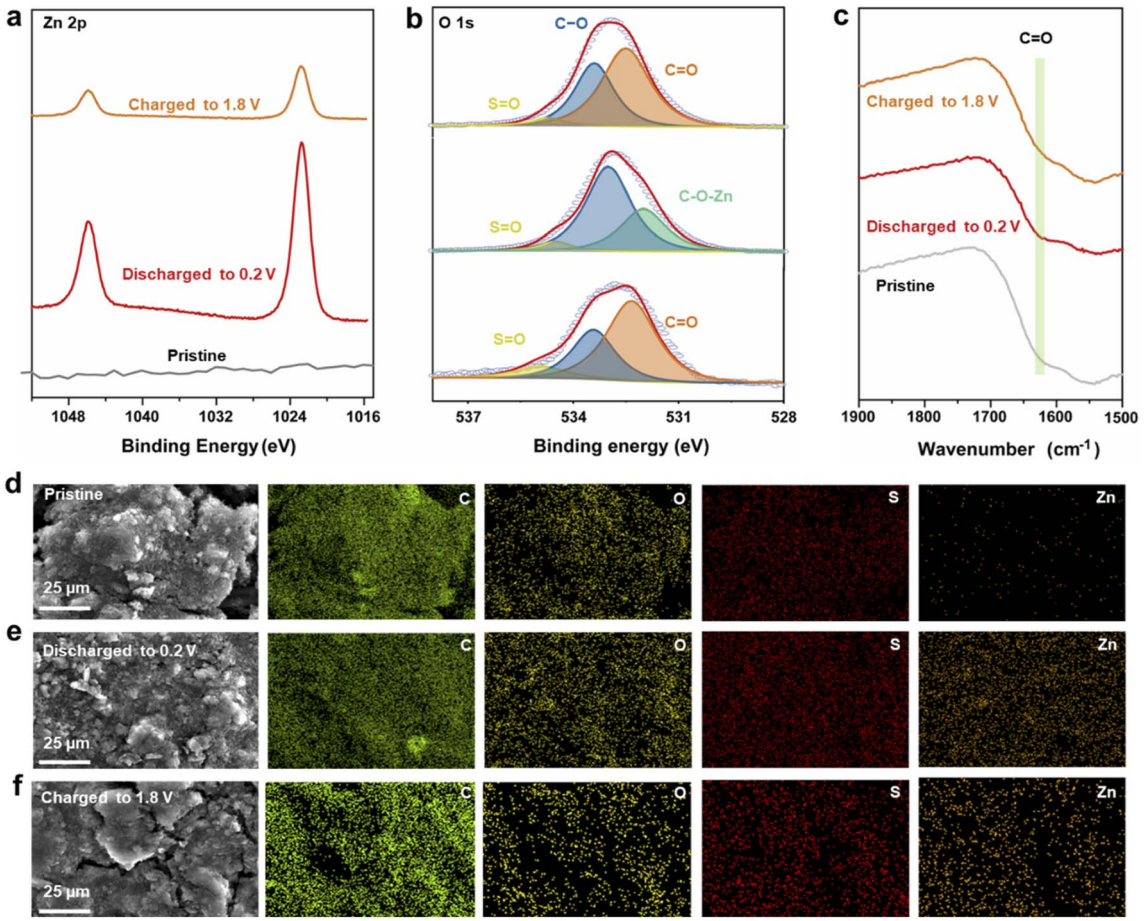

Fig. 3 (a) *Ex situ* XPS spectra of the various valence levels of Zn element in different states. (b) XPS spectra of O 1s. (c) *Ex situ* FT-IR spectra of the PPAAQS cathode in various states. (d–f) SEM-EDS pictures of elements distributed among the PPAAQS cathode in various states.

(pH = 5), indicating substantial H^+ participation in this process (Fig. S10c). These results suggest that the electrochemical reaction of PPAAQS involves a Zn^{2+}/H^+ co-storage mechanism, in which the low-potential redox process is dominated by Zn^{2+} insertion/extraction, while the high-potential redox couple is likely associated with proton-coupled electron transfer involving reversible H^+ insertion/extraction.[17,33,34] Moreover, PPAAQS exhibits significantly higher peak currents and a larger integrated CV area than the non-sulfonated polymer PPAAQ, indicating enhanced electrochemical activity and improved utilization of carbonyl active sites.[20,35] These results demonstrate that polymerization effectively improves the structural stability of anthraquinone-based electrodes, while sulfonation further enhances the redox activity through simultaneous regulation of the electronic structure and ion-storage behavior.

The galvanostatic charge–discharge (GCD) curves at 50 mA g^{-1} reveal that PPAAQS delivers a significantly higher specific capacity and more distinct voltage plateaus than PPAAQ (Fig. 2b). The well-defined discharge/charge plateaus are highly consistent with the redox peaks observed in the CV curves, suggesting a highly reversible carbonyl redox reaction in the PPAAQS electrode. The kinetic advantage of PPAAQS becomes more evident under high-rate conditions. As shown in Fig. 2c, PPAAQS delivers reversible capacities of 108.5, 90.2, 76.5, 64.3, 57.4, 51.8, 45.5, and 42.2 mAh g^{-1} at current densities of 0.05, 0.1, 0.2, 0.5, 1, 2, 5, and 10 A g^{-1} respectively. Notably, approximately 39% of the initial capacity is retained even when the current density increases from 0.05 to 10 A g^{-1}, demonstrating excellent rate capability and rapid reaction kinetics. When the current density is switched back to 0.05 A g^{-1}, the discharge capacity rapidly recovers to 101.8 mAh g^{-1}, corresponding to a capacity recovery of 93.8%, indicating excellent structural reversibility and electrochemical robustness. The superior rate performance suggests that the introduction of sulfonic acid groups effectively facilitates charge transfer and ion diffusion, thereby improving the redox reversibility of carbonyl active sites.[36,37]

As shown in Fig. 2d, the long-term cycling stability was evaluated at a current density of 1.0 A g^{-1}. The PPAAQS cathode delivers an initial specific capacity of 60 mAh g^{-1}, retaining 48 mAh g^{-1} after 7100 cycles with 99.95% high coulombic efficiency (CE), corresponding to 80.4% retention and an exceptionally low per-cycle decay rate of just 0.00276%. The nearly constant CE throughout cycling indicates highly reversible Zn^{2+} storage chemistry and excellent electrochemical stability of the polymer framework. In sharp contrast, the PPAAQ cathode

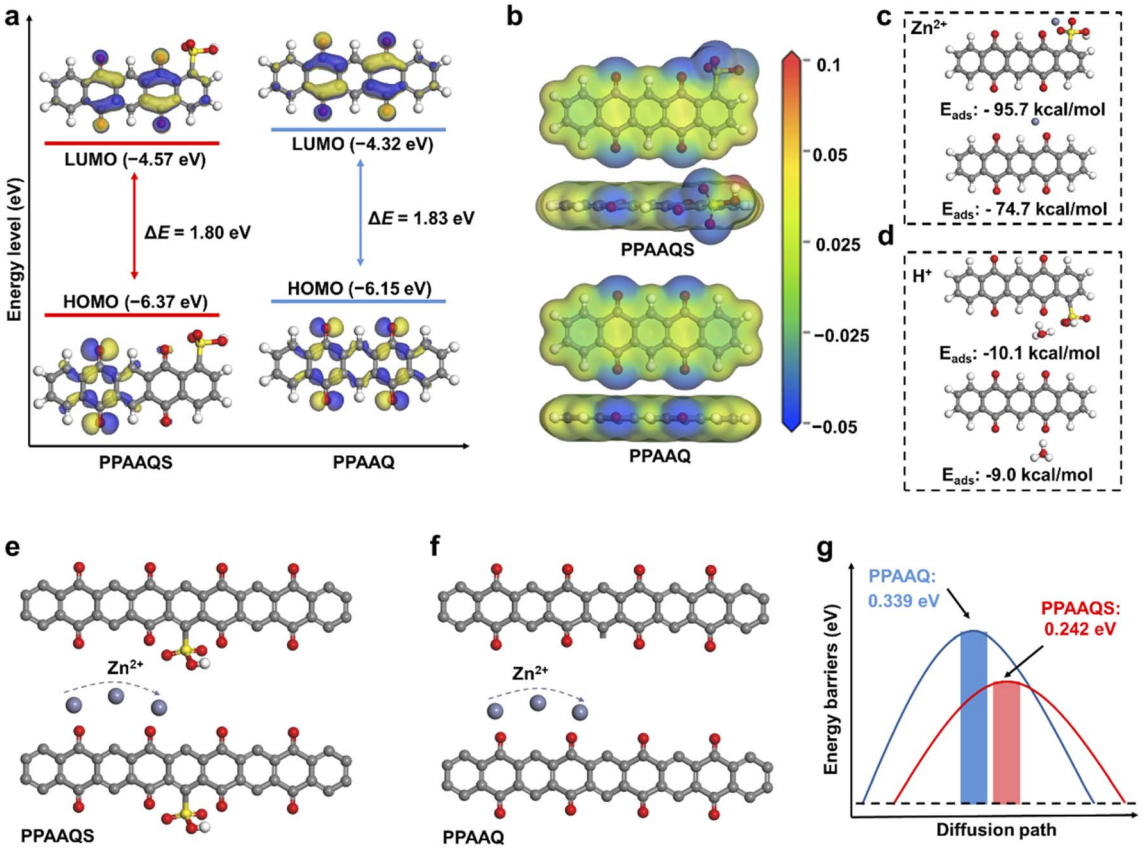

Fig. 4 (a) HOMO and LUMO energy levels, (b) ESPs, and (c) Zn^{2+} ion and (d) proton adsorption energies of the PPAAQS and PPAAQ unit configuration by DFT simulation. The schematic illustration of Zn^{2+} ions diffusion path along carbonyl active sites in (e) PPAAQS and (f) PPAAQ electrodes, (g) corresponding to Zn^{2+} ions diffusion barrier, respectively.

suffers from severe capacity degradation, with over 50% capacity loss after only 860 cycles, ultimately leading to cell failure. To the best of our knowledge, the cycling stability of the PPAAQS cathode compares favorably with the most advanced organic cathodes reported in the literature (Fig. 2e). For instance, the recently reported DHTAT cathode retains 94% of its capacity after only 100 cycles at 1.0 A g^{-1}; TP-Se delivers 85.3% retention after 4300 cycles at 2.0 A g^{-1}; and TDT exhibits 82% retention after 3000 cycles at 10.0 A g^{-1}, all of which are inferior to the PPAAQS cathode in terms of either cycle number, capacity retention, or per-cycle decay rate. The corresponding data are summarized in Table S2.

As shown in Fig. 2d, the long-term cycling stability was evaluated at a current density of 1.0 A g^{-1}. The PPAAQS cathode delivers an initial specific capacity of 60 mAh g^{-1}, retaining 48 mAh g^{-1} after 7100 cycles with 99.95% high coulombic efficiency (CE), corresponding to 80.4% retention and an exceptionally low per-cycle decay rate of just 0.00276%, compared to previously reported results (Fig. 2e and Table S2). The nearly constant CE throughout cycling indicates highly reversible Zn^{2+} storage chemistry and excellent electrochemical stability of the polymer framework. In sharp contrast, the PPAAQ cathode suffers from severe capacity degradation, with over 50% capacity loss after only 860 cycles, ultimately leading to cell failure. Self-discharge tests were carried out for PPAAQS||Zn and PPAAQ||Zn cells after fully charging to the same state of charge (Fig. S11). After resting for 24 h, the PPAAQ||Zn cell retained a voltage of only 0.99 V with a CE of 87.2%, while the PPAAQS||Zn cell maintained a higher voltage of 1.08 V and achieved a significantly elevated CE of 98.3%, which further confirm that sulfonation effectively suppresses spontaneous redox reactions and enhances the electrochemical stability of PPAAQS. To demonstrate the practical applicability of the PPAAQS cathode, we assembled a Zn||PPAAQS pouch cell with a PPAAQS cathod mass loading of 10 mg cm^{-2} (size: 8 × 5 cm). This cell can power a small fan (Fig. 2f) and delivers stable cycling performance over 380 cycles with a capacity retention of 78.6% (Fig. 2g).

The rapid capacity fading suggests severe kinetic deterioration and interfacial instability during repeated charge/discharge processes. To gain further insights into the interfacial electrochemical kinetics, electrochemical impedance spectroscopy (EIS) measurements were conducted before and after long-term cycling. As shown in Fig. S12a, the pristine PPAAQS electrode exhibits a much smaller semicircle diameter than PPAAQ, indicating significantly reduced charge-transfer resistance at the electrode/electrolyte interface.[38] The reduced charge-transfer resistance demonstrates that the introduction of sulfonic acid groups facilitates interfacial electron transfer and improves the electrochemical accessibility of carbonyl

 This journal is © The Royal Society of Chemistry 2026

active sites. The lower interfacial resistance suggests that the introduction of sulfonic acid groups facilitates electron transfer during the carbonyl redox reaction and improves the accessibility of electrochemically active sites.[39] The evolution of impedance after prolonged cycling provides more direct evidence for the beneficial role of sulfonation. As shown in Fig. S12b–d, the PPAAQS electrode maintains a relatively small semicircle even after 1000 cycles, indicating that the charge-transfer kinetics remain highly stable during repeated Zn^{2+} insertion/extraction processes. In contrast, PPAAQ exhibits a dramatically enlarged semicircle after cycling, indicating a substantial increase in charge-transfer resistance. The continuous growth of interfacial resistance is highly consistent with the rapid capacity fading observed during long-term cycling, indicating progressive kinetic degradation of the PPAAQ electrode. Contact-angle measurements reveal a dramatic improvement in electrolyte wettability after sulfonation (Fig. S13a). The contact angle decreases from 38° for PPAAQ to only 8° for PPAAQS, indicating substantially enhanced affinity toward the aqueous electrolyte. Such ultralow contact angle enables rapid electrolyte infiltration into the electrode and facilitates access of Zn^{2+} ions to the redox-active carbonyl sites. Therefore, the EIS and contact-angle results consistently demonstrate that sulfonation effectively optimizes the electrode/electrolyte interface, which plays a crucial role in enabling the enhanced rate capability and exceptional cycling stability of PPAAQS.

To quantitatively evaluate ion-transport kinetics, galvanostatic intermittent titration technique (GITT) measurements were conducted. As shown in Fig. 2h, PPAAQS exhibits significantly smaller voltage polarization during both discharge and charge processes than PPAAQ, indicating reduced electrochemical polarization and enhanced reaction kinetics associated with Zn^{2+} insertion/extraction (Fig. S14).[40] The corresponding Zn^{2+} diffusion coefficients ($D_{Zn^{2+}}$) values of PPAAQS and PPAAQ are in the range of 10^{-8}–10^{-9} cm^2 s^{-1} and the $D_{Zn^{2+}}$ of the PPAAQS ($\sim 10^{-8}$ cm^2 s^{-1}) is significantly higher than the PPAAQ ($\sim 10^{-9}$ cm^2 s^{-2}) in both charge and discharge processes (Fig. 2i). The enhanced Zn^{2+} diffusion behavior can be attributed to the hydrophilic sulfonated framework, which facilitates electrolyte penetration and establishes continuous ion-transport pathways within the polymer electrode.[41] Combined with the contact-angle and EIS results, the GITT analysis demonstrates that sulfonation effectively reduces both interfacial transport resistance and bulk ion-diffusion barriers, thereby enabling rapid Zn^{2+}/H^+ migration during cycling.

The energy storage mechanism was further investigated by *ex situ* XPS analysis. As shown in Fig. 3a, no Zn 2p signal is observed in the pristine PPAAQS electrode. Upon discharge to 0.2 V, characteristic Zn 2p peaks emerge at approximately 1022 and 1045 eV, confirming Zn^{2+} insertion into the polymer host. The intensity of Zn 2p signals decreases substantially upon recharging to 1.8 V, indicating reversible Zn^{2+} extraction from the polymer host. Simultaneously, in high-resolution O 1s XPS spectrum (Fig. 3b), the characteristic peak of C=O group disappeared at the fully discharged state and rose again to a high level at the fully charged state, indicating the reversible conversion between C=O and C–O group in the polymer. Meanwhile, a new C–O–Zn peak was detected in the fully discharged state, which further verifies the Zn^{2+}-coordination with carbonyl groups in the polymer framework during the discharged process.[42] Furthermore, the FT-IR spectra confirm that PPAAQS maintains an intact molecular structure under both fully charged and fully discharged states (Fig. 3c).[24] The O 1s peak assigned to the S=O bond of sulfonic acid groups (~535.8 eV) exhibits negligible changes in both binding energy and peak intensity after discharging to 0.2 V and subsequent recharging to 1.8 V (Fig. 3b). This observation confirms that sulfonate moieties remain electrochemically inert and structurally stable throughout cycling, acting as stable ion-conductive channels rather than participating in redox reactions. As shown in Fig. 3d–f, SEM-EDS mapping was also employed to look into the charging/discharging process of PPAAQS. It was further shown that Zn^{2+} ions are reversibly inserted/extracted from the PPAAQS cathode throughout the charge/discharge cycle by contrasting the distribution of C, O, S, and Zn elements.

Further evaluate the interfacial stability during cycling, the cathodes after 100 cycles were characterized by SEM, EDS mapping, and XRD analyses. As shown in Fig. S15 and S16, both electrodes maintain their overall morphology, while the elemental mapping confirms the homogeneous distribution of C, O, S, and Zn elements. Notably, the PPAAQ electrode exhibits more pronounced surface deposits after cycling. XRD patterns (Fig. S17) reveal the formation of $Zn_4(OH)_6SO_4 \cdot 5H_2O$ (ZHS) on both electrodes, which originates from local pH fluctuations during the electrochemical process.[43] However, the characteristic ZHS diffraction peaks are significantly weaker for PPAAQS than for PPAAQ, indicating suppressed by-product formation. This result can be attributed to the introduction of sulfonic acid groups, which regulate the local interfacial microenvironment and alleviate local alkalization during cycling.[44] Consequently, enabled by the modulation of the interfacial microenvironment *via* sulfonic acid groups, PPAAQS efficiently restrains the irreversible deposition of ZHS byproducts and preserves a stable, low-impedance electrode–electrolyte interface (Fig. S17, S12b and c). In comparison, severe ZHS precipitation occurs on the PPAAQ electrode upon cycling (Fig. S17). The progressive coverage of active sites by byproducts drives a persistent rise in interfacial charge-transfer resistance and gradual site passivation, resulting in rapid capacity decay and markedly reduced cycling lifespan (Fig. 2d).

To further elucidate the molecular origin of the enhanced electrochemical performance, density functional theory (DFT) calculations were performed to probe the influence of sulfonic acid groups on both the electronic structure and ion-interaction behavior of the polymer frameworks. We first compared the lowest unoccupied molecular orbital (LUMO) and highest occupied molecular orbital (HOMO) energy levels of PPAAQS and PPAAQ. As shown in Fig. 4a, the LUMO level of PPAAQS (−4.57 eV) is markedly lower than that of PPAAQ (−4.32 eV), indicating that electron injection into the carbonyl redox centers becomes thermodynamically more favorable upon sulfonation.[45] This reduced LUMO energy is consistent with the positive shift of the redox peaks observed in the CV curves

(Fig. S9), providing theoretical support for the enhanced redox kinetics. Meanwhile, the slightly narrowed bandgap (E_g = 1.80 eV for PPAAQS *vs.* 1.83 eV for PPAAQ) suggests a modest improvement in intrinsic electronic conductivity, which may facilitate charge transport within the polymer matrix. Beyond electronic modulation, the electrostatic potential (ESP) mapping in Fig. 4b reveals a pronounced increase in localized negative charge density around both the carbonyl oxygen atoms and the sulfonate ($-SO_3^-$) groups of PPAAQS. This electron-rich environment creates stronger electrostatic binding sites for cation adsorption (−10.1 kcal mol^{-1} for PPAAQS *vs.* −9.0 kcal mol^{-1} for PPAAQ, Fig. 4d).

Quantitatively, the calculated Zn^{2+} adsorption energy (E_{ads}) becomes more negative after sulfonation (−95.7 kcal mol^{-1} for PPAAQS *vs.* −74.7 kcal mol^{-1} for PPAAQ, Fig. 4c). This stronger affinity facilitates the pre-concentration of Zn^{2+} ions in the vicinity of carbonyl active sites, effectively lowering the activation energy for the subsequent interfacial electron transfer. Concurrently, the sulfonated framework reduces the Zn^{2+} migration barrier along the ion-transport pathway from 0.339 eV (PPAAQ, Fig. 4f) to 0.242 eV (PPAAQS, Fig. 4e), indicating accelerated bulk ion diffusion (Fig. 4g). These theoretical predictions are corroborated by the significantly higher Zn^{2+} diffusion coefficients derived from GITT measurements (Fig. 2i) and the smaller charge-transfer resistance observed in EIS (Fig. S12a) for PPAAQS. Therefore, the reduced charge-transfer energy consumption in PPAAQS can be rationalized by the synergistic effect of sulfonation on both adsorption energetics and ion migration.

Collectively, these theoretical and experimental results establish a coherent picture of sulfonation-induced electron/ion dual regulation. Electronically, the electron-withdrawing sulfonate groups lower the LUMO level and activate carbonyl redox centers, facilitating charge transfer with reduced polarization. Ionically, the hydrophilic sulfonated framework enhances wettability, strengthens Zn^{2+} coordination, and creates transport pathways for both Zn^{2+} and H^+, as evidenced by the lowered diffusion barrier and proton-coupled redox participation. This synergistic optimization simultaneously reduces charge-transfer resistance, ion-diffusion barriers, and polarization, endowing the PPAAQS cathode with high capacity, superior rate capability, and exceptional long-term cycling stability.

Conclusion

In summary, we have successfully developed a sulfonated anthraquinone-based polymer (PPAAQS) as robust cathode for aqueous zinc-ion batteries through molecular sulfonation engineering. Comprehensive experimental and theoretical analyses collectively demonstrate that the covalently tethered sulfonic acid groups serve a dual regulatory function: electronically, they lower the LUMO energy level and enhance Zn^{2+} affinity toward the carbonyl redox centers, facilitating charge transfer; ionically, they improve electrolyte wettability, construct continuous ion-transport pathways, and stabilize the electrode/electrolyte interface. DFT calculations further reveal that the sulfonated framework optimizes the adsorption energetics and reduces diffusion barriers for both Zn^{2+} and H^+, thereby promoting synergistic dual-ion transport kinetics. Benefiting from this integrated electron/ion dual regulation, the PPAAQS cathode delivers outstanding rate capability, retaining ∼39% of its initial capacity when the current density increases from 0.05 to 10 A g^{-1}, along with exceptional long-term cycling stability (80.4% capacity retention after 7100 cycles at 1 A g^{-1}). This work establishes molecular sulfonation engineering as an effective approach that simultaneously optimizes the electronic structure and ion-transport behavior of organic cathodes. We anticipate that this strategy can be extended to other carbonyl-based organic electrode materials and inspire further molecular-level designs toward durable and high-performance aqueous zinc-ion batteries.

Experimental

Reagents

Pyromellitic dianhydride (PMDA), anthraquinone (AQ), sodium anthraquinone-1-sulfonate (AQS), aluminum chloride ($AlCl_3$), sodium chloride (NaCl), hydrochloric acid, acetone, and 1-methyl-2-pyrrolidinone (NMP). All starting chemicals and solvents were purchased from commercial sources and used without further purification.

Synthesis of materials

PPAAQ and PPAAQS were synthesized *via* Friedel–Crafts polymerization by a molten salt sulfonation method.[26] Firstly, the mixture of $AlCl_3$ and NaCl (a molar ratio of 2 : 1) was heated at 160 °C to produce a liquid fused salt. Secondly, 5 mmol pyromellitic dianhydride (PMDA) and 5 mmol anthraquinone (AQ) were introduced into the fused salt and then heated at 250 °C with continuously stirring for 2 h. After cooling to room temperature, the reaction solution was poured into deionized water for precipitation; the precipitate was filtered, washed repeatedly with deionized water and ethanol, and vacuum-dried to obtain the PPAAQ blank powder. The synthetic procedure of PPAAQS is consistent with that of PPAAQ. Specifically, AQ monomer was replaced with sodium anthraquinone-1-sulfonate (AQS). After the PPAAQS product was obtained, it was further subjected to proton exchange in 1 M and 0.1 M HCl aqueous solutions for 24 h, respectively. Subsequently, the material was rinsed with a large amount of deionized water to remove residual hydrochloric acid. Eventually, the sample was gathered and dried under a vacuum at 80 °C.

Materials characterization

The micromorphology and chemical structure of PPAAQ and PPAAQS were characterized by scanning electron microscopy (SEM, FEI Sirion), high-resolution transmission electron microscope (HRTEM, Talos P200X G2), Fourier transform infrared spectrometer (FTIR, SCIENTIFIC iS10), X-ray diffraction (XRD, Bruker D8), X-ray photoelectron spectrometer (XPS, Shimadzu AXIS SUPRA+), Optical Contact Angle Goniometer (FTIR, LAUDA Scientific OSA 100), and Elemental Analyzer

 This journal is © The Royal Society of Chemistry 2026

(Elementar vario EL cube), Thermogravimetric analyzer (TGA, NETZSCH TG209 F3).

Electrochemical measurements

Electrochemical characterization of full cells was conducted using 2032-type coin-cells with 2.0 M $ZnSO_4$ as electrolyte. The glass fiber (GF) separator was purchased from Whatman, model GF-D. For assembling full cells, the cathodes were prepared by first mixing the active material (PPAAQ and PPAAQS) with carbon black and polytetrafluoroethylene in a mass ratio of 7 : 2 : 1 to form a homogenous ink. Then the ink was cast onto a carbon paper, followed by drying at 80 °C under vacuum for 12 h. After that, the dried electrodes were punched into disks with a diameter of 10 mm, and assembled into coin cells with 12 mm-diameter separators, 10 mm-diameter and 20 μm thick Zn foils or other corresponding electrode materials. The mass loading of active materials in coin-type cells was controlled at approximately 2 mg cm^{-2}. Galvanostatic charge–discharge, cycling rate performance, and long-term cycling were tested by LAND-3002A. The linear sweep voltammetry and cyclic voltammetry (CV) curves measurements were carried out by AUTOLAB-PGSTAT302N. For ionic conductivity measurements at room temperature (25 °C), different samples were sandwiched between two SS electrodes, and impedance measurements were performed using the PGSTAT302N electrochemical workstation.

Computational methods

Density functional theory (DFT) calculations were performed using the DMol3 module. The generalized gradient approximation (GGA) with the Perdew Burke–Ernzerhof (PBE) functional was employed for geometry optimization and electronic structure calculations. The double numerical plus polarization (DNP) basis set was selected, and all structures were fully optimized before further calculations.

The frontier molecular orbital energies of PPAAQ and PPAAQS were calculated to investigate the influence of sulfonation on the electronic structure. The adsorption energies (E_{ads}) of Zn^{2+} and H^+ on different functional sites were calculated using (1):

$$E_{ads} = E_{complex} - E_{substrate} - E_{ion} \quad (1)$$

where $E_{complex}$, $E_{substrate}$, and E_{ion} represent the total energies of the ion-adsorbed system, pristine polymer, and isolated ion, respectively.

The transition state (TS) and minimum energy pathways for the Zn^{2+} diffusion was searched using the synchronous transit methods. Frequency analysis was subsequently conducted to confirm that the optimized TS structure possessed only one imaginary frequency, and the corresponding vibrational mode correctly represented the intended migration pathway. The diffusion barrier was calculated as (2):

$$E_d = E_{TS} - E_{initial} \quad (2)$$

where E_{TS} and $E_{initial}$ represent the energies of the transition state and initial state, respectively.

Conflicts of interest

The authors declare no conflict of interest.

Data availability

The raw data including X-ray diffraction patterns, electrochemical measurements, DFT calculation results and other analysis data that support the findings of this work are available from the corresponding author upon reasonable request.

Supplementary information (SI): the structural and morphological characterizations, electrochemical data, and other analysis data. See DOI: https://doi.org/10.1039/d6ta05865e.

Acknowledgements

This work was financially supported by the National Natural Science Foundation of China (grant no. 52371214, 52302224, 52171203), the Natural Science Foundation of Jiangsu Province (grants no. BK20211516), the Scientific Research Beidou Project of Nanjing Polytechnic Institute (NJPI-RC-2024-12).

Notes and references

1 S. Yang, A. Chen, Z. Tang, Z. Wu, P. Li, Y. Wang, X. Wang, X. Jin, S. Bai and C. Zhi, *Energy Environ. Sci.*, 2024, **17**, 1095–1106.
2 J. L. Yang, M. Du, J. M. Cao and X. L. Wu, *Angew. Chem., Int. Ed.*, 2026, **65**, e7123448.
3 R. Zhang, W. K. Pang, J. Vongsvivut, J. A. Yuwono, G. Li, Y. Lyu, Y. Fan, Y. Zhao, S. Zhang, J. Mao, Q. Cai, S. Liu and Z. Guo, *Energy Environ. Sci.*, 2024, **17**, 4569–4581.
4 X. Zheng, H. Zhu, Z. Wang, H. Yang, R. Li, W. Luo, W. H. Kan, Y. Dai, H. Zhang, J. Wang, H. Cui, X. Fan, C. Zhi and Y. Huang, *Nat. Nanotechnol.*, 2026, **21**, 95–105.
5 Z. Y. Wu, F. Ye, Q. Liu, R. L. J. Pang, Y. Liu, L. Jiang, Z. L. Tang and L. F. Hu, *Adv. Energy Mater.*, 2022, **12**, 2200654.
6 X. Q. Hu, P. F. Wang, Q. Q. Lei, S. Zou, L. L. Du, W. J. Song, M. Zhu, Z. Gong, Y. H. Wu, Y. H. Zhang and F. N. Shi, *J. Alloys Compd.*, 2026, **1059**, 187196.
7 Y. Liu, L. Lin, T. Zhang, Z. Xue, J. Liu, D. Chao and X. Sun, *Energy Environ. Sci.*, 2024, **17**, 2521–2529.
8 X. Q. Hu, R. H. Li, L. L. Du, W. J. Song, Q. Q. Lei, S. Zou, P. F. Wang, M. Zhu, Z. Gong, Y. H. Wu, Y. H. Zhang and F. N. Shi, *Electrochim. Acta*, 2025, **542**, 147531.
9 G. Li, L. Sun, S. Zhang, C. Zhang, H. Jin, K. Davey, G. Liang, S. Liu, J. Mao and Z. Guo, *Adv. Funct. Mater.*, 2024, **34**, 2301291.
10 C. Qiu, H. Huang, M. Yang, L. Xue, X. Zhu, Y. Zhao, M. Ni, T. Chen and H. Xia, *Energy Storage Mater.*, 2024, **72**, 103736.
11 Z. Li, J. Tan, Y. Wang, C. Gao, Y. Wang, M. Ye and J. Shen, *Energy Environ. Sci.*, 2023, **16**, 2398–2431.
12 L. Lin, Z. Xue, T. Qiu, J. Zhu, G. Zhang, H. Zhan, K. Wang and X. Sun, *Energy Environ. Sci.*, 2024, **17**, 6499–6506.
13 Y. Yang, Z. Tang, S. Bian, Y. Gu, F. Ye, W. Chen, K. Zhu, Y. Wu and L. Hu, *Adv. Energy Mater.*, 2025, **15**, 2500316.

14 S. Bian, Y. Yang, S. Liu, F. Ye, H. Tang, Y. Wu and L. Hu, *Chem.–Eur. J.*, 2024, **30**, e202303917.
15 Z. Song, W. Liu, Q. Huang, Y. Lv, L. Gan and M. Liu, *Chem. Sci.*, 2025, **16**, 16542–16551.
16 Q. Ma, C. Ji, Z. Wang, R. Wang, L. Zhang, H. Li, Y. Xu, Q. Zhang, D. Chao and C. Zhang, *Energy Environ. Sci.*, 2026, **19**, 3512–3523.
17 X. Ma, Y. Gao, Y. Wang, Y. Chen, F. Lin, Z. Zhang, H. Zhang and P. Gu, *Adv. Funct. Mater.*, 2026, **36**, e75643.
18 C. Ye, X. Zhou and S. Tang, *Angew. Chem., Int. Ed.*, 2025, **64**, e202501743.
19 Y. Wang, H. Cui, R. Li, C. Yue, H. Pan, Z. Tang, X. Wang, Y. Lin, H. Li, C. Han, D. Nan, C. Zhi and H. Lv, *Energy Storage Mater.*, 2024, **65**, 103102.
20 Y. Li, Y. Hou, Z. Liu, B. Mei and H. Niu, *Langmuir*, 2025, **41**, 11443–11453.
21 C. Li, X. Zhang, W. He, G. Xu and R. Sun, *J. Power Sources*, 2020, **449**, 227596.
22 Z. Tie and Z. Niu, *Angew. Chem., Int. Ed.*, 2020, **59**, 21293.
23 J. Xu, Y. Yang, Q. Dai, Z. Zheng, Y. Cao, Y. Cheng, B. Peng, L. Ma and Y. Wang, *Angew. Chem., Int. Ed.*, 2025, **64**, e202423118.
24 X. Shi, S. Chen, H. Yu, Q. Zong, K. Ding, Y. Wang, D. Xu, S. Xu and Z. Chen, *Nano Lett.*, 2025, **25**, 13326–13333.
25 M. Zhu, S. Ku, Q. Ran, H. Huang, N. Cao, F. Bai, X. Lang, D. Chao and M. Feng, *Energy Environ. Sci.*, 2026, **19**, 3629–3639.
26 F. Ye, Q. Liu, H. Dong, K. Guan, Z. Chen, N. Ju and L. Hu, *Angew. Chem., Int. Ed.*, 2022, **61**, e202214244.
27 F. Ye, X. Zhang, K. Liao, Q. Lu, X. Zou, R. Ran, W. Zhou, Y. Zhong and Z. Shao, *J. Mater. Chem. A*, 2020, **8**, 9733–9742.
28 R. Wang, Y. Zhang, C. Ma, X. Wang, M. Cai, H. Du, Z. Yang, D. Chao and Y. Wang, *Adv. Funct. Mater.*, 2025, **35**, 2505318.
29 G. Wu, S. J. Lin, I. C. Hsu, J. Y. Su and D. W. Chen, *Polymers*, 2019, **11**, 1177.
30 C. Guo, Y. Liu, J. Zhang, W. Zhao, K. Wang, M. Su, Y. Hu and L. Wang, *Ionics*, 2023, **29**, 2319–2328.
31 N. He, Y. Zou, C. Chen, M. Tan, Y. Zhang, X. Li, Z. Jia, J. Zhang, H. Long, H. Peng, K. Yu, B. Jiang, Z. Han, N. Liu, Y. Li and L. Ma, *Nat. Commun.*, 2024, **15**, 3896.
32 C. Wang, Y. Tian, W. Chen, X. Lin, J. Zou, D. Fu, X. Yu, R. Qiu, J. Qiu and S. Zeng, *Polymers*, 2024, **16**, 687.
33 L. Huang, J. Li, X. Gao, Y. Wang, H. Xie, H. Liang, G. Wang and T. Gu, *Chem. Eng. J.*, 2025, **513**, 162993.
34 Y. Chen, J. Li, Q. Zhu, K. Fan, Y. Cao, G. Zhang, C. Zhang, Y. Gao, J. Zou, T. Zhai and C. Wang, *Angew. Chem., Int. Ed.*, 2022, **61**, e202116289.
35 Z. M. Jiang, T. T. Xu, C. C. Yan, C. Y. Ma and S. G. Dai, *Front. Chem.*, 2018, **6**, 00431.
36 Y. Wang, H. Zhou, S. Wei, S. Chen, D. Cao, Q. Zhou, X. Wu and L. Song, *J. Am. Chem. Soc.*, 2025, **147**, 41297–41307.
37 Y. Zhang, Q. Huang, Z. Song, L. Miao, Y. Lv, L. Gan and M. Liu, *Adv. Funct. Mater.*, 2024, **35**, 2416415.
38 G. Zhou, C. Tang, X. Tang, T. Wang, C. Zhao, C. Liu, X. Xu, S. Wang, T. Miao, L. Xu, Y. Yan, Z. Wang, L. Zhang and J. Zhu, *Adv. Energy Mater.*, 2026, **16**, e05264.
39 Y. Cao, W. Sun, C. Guo, L. Zheng, M. Yao and Y. Wang, *ACS Nano*, 2022, **16**, 9830–9842.
40 B. Wang, S. Sun, B. Wu and K. Huang, *ACS Electrochem.*, 2026, **2**, 197–207.
41 H. Hong, X. Yang, Y. Wang, Z. Wei, D. Li, X. Guo, Y. Wang, Q. Nian, S. Zhang, S. Wang, S. Wang, S. Li, D. Zhang, Q. Xiong, H. Yang and C. Zhi, *Nat. Commun.*, 2026, **17**, 4933.
42 C. Li, L. Hu, X. Ren, L. Lin, C. Zhan, Q. Weng, X. Sun and X. Yu, *Adv. Funct. Mater.*, 2024, **34**, 2313241.
43 N. Jiang, Y. Zeng, Q. Yang, P. Lu, K. Qu, L. Ye, X. Lu, Z. Liu, X. Li, Y. Tang, J. Cao, S. Chen, C. Zhi and J. Qiu, *Energy Environ. Sci.*, 2024, **17**, 8904–8914.
44 G. Lai, X. Hu, S. Liang, Y. Yang, E. R. Elsharkawy, G. A. M. Mersal, B. Lu, Z. M. El-Bahy, Y. Liu and J. Zhou, *ACS Energy Lett.*, 2025, **10**, 3437–3444.
45 L. Li, H. Yang, X. Wang, Y. Ma, W. Ou, H. Peng and G. Ma, *J. Mater. Chem. A*, 2023, **11**, 26221–26229.

 This journal is © The Royal Society of Chemistry 2026